Preprint typeset using LaTeX style emulateapj v. 11/12/01

SPATIAL STUDY WITH THE VLT OF A NEW RESOLVED EDGE-ON CIRCUMSTELLAR DUST DISK DISCOVERED AT THE PERIPHERY OF THE ρ OPHIUCHI DARK CLOUD[1]

N. Grosso[2], J. Alves[3], K. Wood[4], R. Neuhäuser[2], T. Montmerle[5], and J. E. Bjorkman[6]

ABSTRACT

We report the discovery in near-infrared (NIR) with SofI at the *New Technology Telescope* (NTT) of a resolved circumstellar dust disk around a 2MASS source at the periphery of the ρ Ophiuchi dark cloud. We present follow-up observations in J, H, and K_s-band obtained with ISAAC at the *Very Large Telescope* (VLT), under $0\farcs4$-seeing conditions, which unveil a dark dust lane oriented East-West between two characteristic northern and southern reflection nebulae. This new circumstellar dust disk has a radius of $2\farcs15$ (300 AU at 140 pc), and a width of $1\farcs2$ (170 AU at 140 pc). Thanks to its location at the periphery of the dense cores, it suffers small foreground visual extinction ($A_{\rm V} = 2.1 \pm 2.6$ mag). Although this disk is seen close to edge-on, the two reflection nebulae display very different colors. We introduce a new NIR data visualization called "Pixel NIR Color Mapping" (PICMap for short), which allows to visualize directly the NIR colors of the nebula pixels. Thanks to this method we identify a ridge, $0\farcs3$ (40 AU at 140 pc) to the north of the dark lane and parallel to it, which displays a NIR color excess. This ridge corresponds to an unusual increase of brightness from J to $K_{\rm S}$, which is also visible in the NTT observation obtained 130 days before the VLT one. We also find that the northern nebula shows $\sim$3 mag more extinction than the southern nebula. We compute axisymmetric disk models to reproduce the VLT scattered light images and the spectral energy distribution (SED) from optical to NIR. Our best model, with a disk inclination $i = 86 \pm 1°$, correctly reproduces the extension of the southern reflection nebula, but it is not able to reproduce either the observed NIR color excess in the northern nebula or the extinction difference between the two reflection nebulae. We discuss the possible origin of the peculiar asymmetrical NIR color properties of this object.

Subject headings: Open clusters and association: individual: ρ Ophiuchi dark cloud —infrared: stars —Stars: individual: 2MASSI 1628137-243139 —Stars: pre-main sequence —Stars: circumstellar matter —Stars: formation

1. INTRODUCTION

Observations of resolved circumstellar disks around young stars are very important for our understanding of the formation of solar-type stars and planetary systems. Usually the large difference of brightness between the central star and its circumstellar material does not allow direct imaging of the circumstellar disk. However when the disk midplane is seen close to edge-on, models predict that the direct light of the star is blocked out while a small amount of the light is scattered by the grains below and above the disk midplane, producing a typical pattern of a dark lane between two reflection nebulae (Whitney & Hartmann 1992). The first young stellar object displaying this typical pattern, HH 30 IRS in the Taurus dark cloud, was imaged by the HST/WFPC2 (Burrows et al. 1996). Edge-on disks have since become accessible to ground-based NIR observations thanks to adaptive optics or speckle imaging (e.g., observations of HK Tau/c; Stapelfeldt et al. 1998; Koresko 1998). Recently new observations of edge-on disks were reported in one of the nearest star-forming regions, the ρ Ophiuchi dark cloud (L1688; $d \sim 140$ pc), both by the VLT/ISAAC under $0\farcs35$-seeing conditions (Brandner et al. 2000) and the HST/NICMOS (Terebey 2001; Allen et al. 2002). These disks are all located in the dense cores of this dark cloud and are deeply embedded (Fig. 1).

During the period April 4–7 2001, five deep NIR pointings were obtained with the NTT/SofI in the ρ Ophiuchi star-forming region (Grosso et al., in preparation), as follow-up of X-ray observations made with Chandra and XMM-Newton. Grosso et al. (2001) already reported the serendipitous discovery of new embedded Herbig-Haro objects in one of these pointings. We focus here on another pointing at the periphery of the ρ Ophiuchi dark cloud (Fig. 1) where we have discovered a new resolved edge-on circumstellar dust disk. We present in §2 the NTT/SofI data and the follow-up observation made with the VLT/ISAAC (Unit Telescope 1; *Antu*) unveiling the shape of this object. We measure its photometry in §3, and discuss the foreground visual extinction in §4. We introduce in §5 the Pixel NIR Color Mapping of the two

[1] Based on observations carried out at the European Southern Observatory, La Silla, Chile, under project 67.C-0325(A), and Paranal, Chile, under service mode project 267.C-5699(A).

[2] Max-Planck-Institut für extraterrestrische Physik, P.O. Box 1312, D-85741 Garching bei München, Germany; ngrosso@xray.mpe.mpg.de

[3] European Southern Observatory, Karl-Schwarzschild-Str. 2, D-85748 Garching bei München, Germany

[4] School of Physics & Astronomy, University of St Andrews, St Andrews, KY16 9SS, Scotland

[5] Service d'Astrophysique, CEA Saclay, F-91191 Gif-sur-Yvette, France

[6] Ritter Observatory, Department of Physics & Astronomy, University of Toledo, OH 43606, USA

nebulae. In §6 axisymmetric models are used to estimate the physical parameters of this disk, and to predict NIR colors. Finally in §7 we discuss the possible origin of the peculiar NIR color properties of this object.

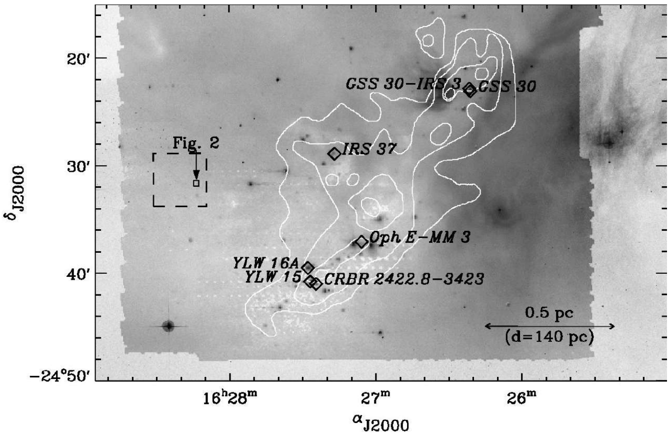

FIG. 1.— Finding chart of the edge-on circumstellar disks in the ρ Ophiuchi dark cloud. The optical background image from the Digitized Sky Survey is merged with the ISOCAM mid-infrared map (6.7 and 14.3 μm; Abergel et al. 1996). The overlaid white contours show the $C^{18}O$ column density (A_V=36, 54, 72, 90 mag; Wilking & Lada 1983), associated with the L1688 dark cloud. Black diamonds mark the previously known young stellar objects displaying in scattered light two reflection nebulae separated by a dark lane (Brandner et al. 2000; Terebey 2001; Allen et al. 2002). They are mostly protostars surrounded by remnant infalling envelopes. The dashed box displays the 5′×5′ field of view of the NTT/SofI pointing at the periphery of the dark cloud. The small square box defines the area of Fig. 2.

2. OBSERVATIONS

2.1. *The NTT/SofI observation*

This observation was made during the night of April 7 at airmass 1.0, with the large SofI field (5′ × 5′; pixel size = 0.″292) to survey the largest area. We took 60 s-exposure frames using 10 s detector sub-integration time to avoid detector non-linearity and saturation. Between each frames the telescope was moved inside a 20″-width box centered on the target position, according to a random pattern of offsets automatically determined by the imaging mode called auto jitter. The net exposure times are 24 min in J, H, and K_S, leading to a K_S∼19 mag completeness magnitude for point sources. The data reduction was performed using the ESO's `eclipse` package (version 3.8.1) which provides the `jitter` command. The best seeing conditions of this NTT/SofI pointing were achieved during the K_S exposure with Full Width at Half Maximum (FWHM) ∼0.″7. The astrometric registration of the reduced images was made using the position of a K_S=14.1 mag star (2MASSI 1628133-243127; Cutri et al. 2000) located only 12″ to the north of our object, extracted using SExtractor (Bertin & Arnouts 1996). J and H images were then resampled to match the K_S image using the `warping` command of `eclipse` with the hyperbolic tangent interpolation kernel.

Figure 2.a shows the resulting color composite image centered on 2MASSI 1628137-243139 which went unnoticed until now. Compared to the unresolved field stars, this source appears extended. One can barely see two characteristic reflection nebulae, and a marginally resolved dark dust lane oriented East-West in front of the star. To confirm this detection and to measure the physical parameters of this disk, we need a deeper and higher angular resolution image. This can easily be achieved with the VLT-UT1/ISAAC, by combining better seeing conditions with better sensitivity and image sampling. We obtained for this goal one hour of the ESO Director's Discretionary Time.

2.2. *The VLT-UT1/ISAAC observation*

The observation was carried out in service mode, triggered by very good seeing conditions (FWHM∼0.″4) on August 15, 2001. The auto jitter imaging mode was also used with 80 s, 60 s, 60 s-exposure frames and 40 s, 15 s, 10 s detector sub-integration time for J, H, and K_S, respectively. Net exposure times were 10 min in K_S and H, and 10.7 min in J, with airmass ranges from 1.05 to 1.11. The data reduction was performed using the version 4.1.0 of `eclipse`. We used the `is_ghost` command to remove the electrical ghosts induced by a bright star in the field of view. The photometric calibration is based on the observation of the IR standard star 9181/S243-E (Persson et al. 1998) provided by the service mode, and taking into account average IR atmospheric extinction on Paranal (0.11, 0.06, and 0.07 mag airmass^{-1} for J, H, and K_S, respectively). We used the same method as described above for our NTT data to produce the resulting color composite image presented in Fig. 2.b (see also the ESO Press Release, Photo 12b/02[7], which presents a larger color composite image corresponding to the field of view shown in Fig. 5).

Thanks to very good seeing conditions and smaller detector pixel size, the two reflection nebulae are unveiled, and the dark dust lane is now clearly resolved in all three filters. The shape of this object seen nearly edge-on and appearing on a starry background has led us to nickname it the *Flying Saucer* (hereafter the FS). Two sources are visible within 2″ (280 AU at 140 pc) of this disk both in the NTT and the VLT images. The first source located at the North-East is the brightest with K_S ∼ 17.5 mag. Stars with similar colors are visible in Fig. 2.b; this source is likely a background star. The second source, thanks to its location close to the South-North disk axis, could be a jet H_2 knot candidate, although no counter knot is visible. Several objects with similar colors and brightnesses are also spread over the field of view, which allows us to interpret this second source also as a background source.

3. PHOTOMETRY OF THE FS

Figure 3 presents the surface brightness maps of the VLT data in the J, H, and K_S-band, respectively, with contours obtained without any smoothing with the Interactive Data Language (`IDL`). We define the dark lane axis as the bisector of the line segment defined by the nebula peaks in the K_S image. The orientation of the dark lane is strictly East-West, and separates the northern and southern reflection nebulae. The southern nebula is slightly asymmetric, with a larger extension towards the East. In J the southern nebula is more extended than its northern counterpart, and the southern peak is 1.7 times brighter than the northern one. This implies that we are not seeing

[7] http://www.eso.org/outreach/press-rel/pr-2002/pr-09-02.html

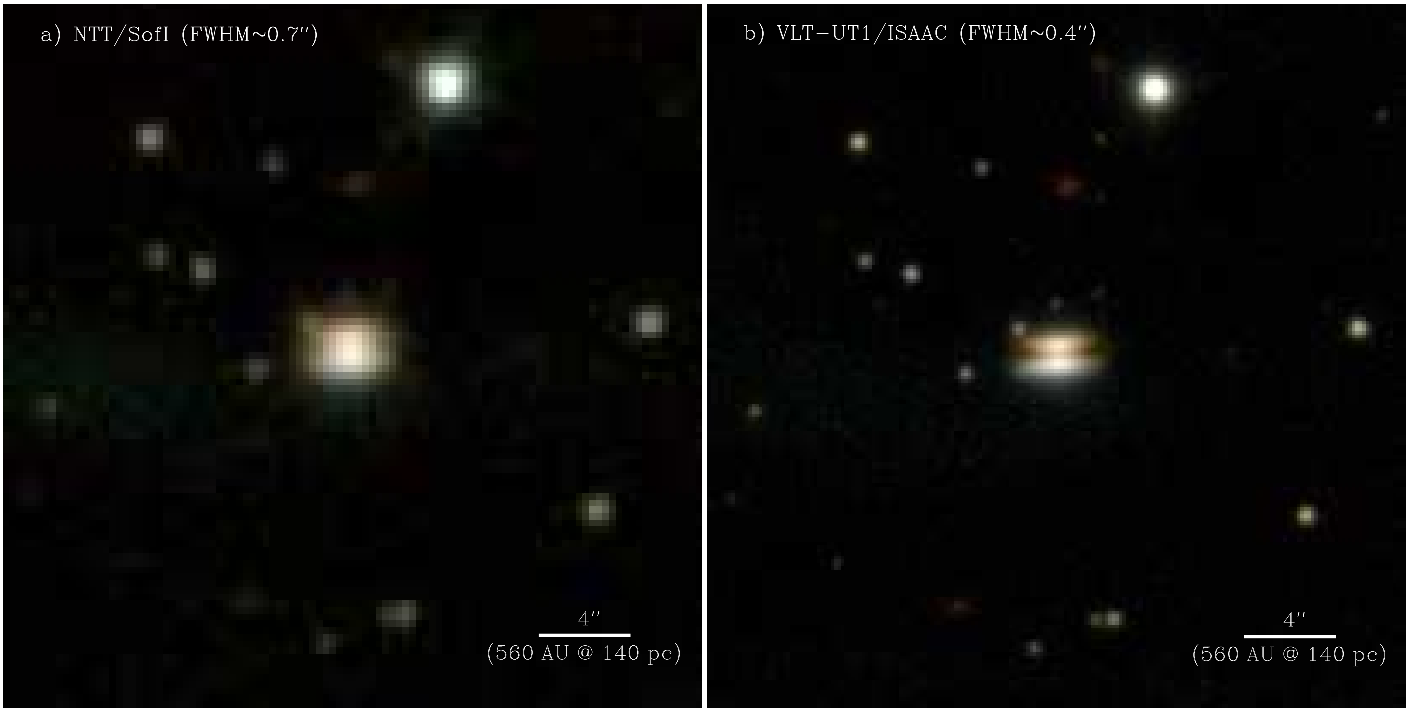

FIG. 2.— Near-infrared view of 2MASSI 1628137-243139. These color composite images combine J, H, and K_S using respectively blue, green, and red color coding, with logarithmic color stretch. The white balance is obtained from the brightest background star. The image size is 30″×30″. The image orientation is North on the top and East on the left hand side. a) observations with the NTT/SofI (pixel size = 0.″292, seeing FWHM∼0.″7). b) observations with the VLT-UT1/ISAAC (pixel size = 0.″148, seeing FWHM∼0.″4).

the FS exactly edge-on. Indeed the scattered light models of accretion disks versus inclination show that when one looks above the disk midplane, the brightness of the upper reflection nebula increases compared to the brightness of the lower reflection nebula (see Whitney & Hartmann 1992). We are therefore seeing the FS slightly below its disk midplane, corresponding to the southern nebula. The difference between the northern and the southern reflection nebula decreases with increasing wavelength, leading to a more symmetric reflection nebulae in K_S. In this filter the northern nebula is still slightly less extended, but its peak brightness is 1.3 times brighter than the southern nebula. This produces the reddish aspect of the northern nebula visible in Fig. 2 both in the NTT and the VLT images. This resolved circumstellar disk has a radius of 2.15″ (300 AU at 140 pc), as measured from the largest extension of the southern nebula (contour 20.4 mag arcsec^{-2} in J), and a width of 1.2″ (170 AU at 140 pc). The shape of the FS, due to its low disk inclination, is reminiscent of HK Tau/c (Stapelfeldt et al. 1998; Koresko 1998), but three times larger and without strong asymmetry in the scattered light intensity.

We compute the photometry of the *integrated light* of the FS using an aperture identical for the three filters, and background estimate from an area free of sources close to the disk. To avoid contamination by the close background star, the aperture photometry is computed from the area where the surface brightness is greater than 19.3 mag arcsec^{-2} in the three filters (see the boundary of the aperture photometry in Fig. 6). The match between the ISAAC filters used here and those used to establish the faint IR standard star system of Persson et al. (1998; a.k.a. the LCO photometric system) being quite good, we use the color transformations given by Carpenter (2001) for the LCO photometric system, to convert the disk magnitudes to the 2MASS photometric system. The resulting J, H, and K_S integrated magnitudes are listed in Table 1. These values are consistent with the values given for 2MASSI 1628137-243139 in Cutri et al. (2000), taking into account the photometry uncertainties. This implies no dramatic change in the brightness of this disk on ∼3 years timescale. However this does not exclude very large changes over a few days like those seen in HH 30 IRS (Wood et al. 2002).

We list also in Table 1 existing complementary integrated magnitudes from other broad-band optical/NIR filters. Using the absolute calibration given by Cox (2000), we obtain the corresponding spectral energy distribution (SED) from optical to NIR presented in Fig. 3. This disk was not detected in the mid-infrared (MIR) by the ISOCAM survey although located in low-noise region of this survey (Bontemps et al. 2001; 6 and 10.5 mJy upper limits for 6.7 and 14.3 μm, respectively, corresponding to the central wavelength of the ISOCAM filters LW2 and LW3). Indeed for edge-on inclinations, all the material of the disk midplane is on the line of sight leading to an optically thick medium in the MIR; continuum emission from the warm inner disk needs deeper exposure times to be detected (see e.g., ISOCAM MIR spectrum of HH 30 IRS; Stapelfeldt & Moneti 1999). The SED shape, rising in the optical and reaching a peak in H, is similar to that of HH 30 IRS (optical variability from Wood et al. 2000; NIR from Cotera et al. 2001; mid-infrared to millimetric from Brandner et al. 2000 and references therein), and consistent with edge-on disk models (e.g. Boss & Yorke 1996; see also below §6.4).

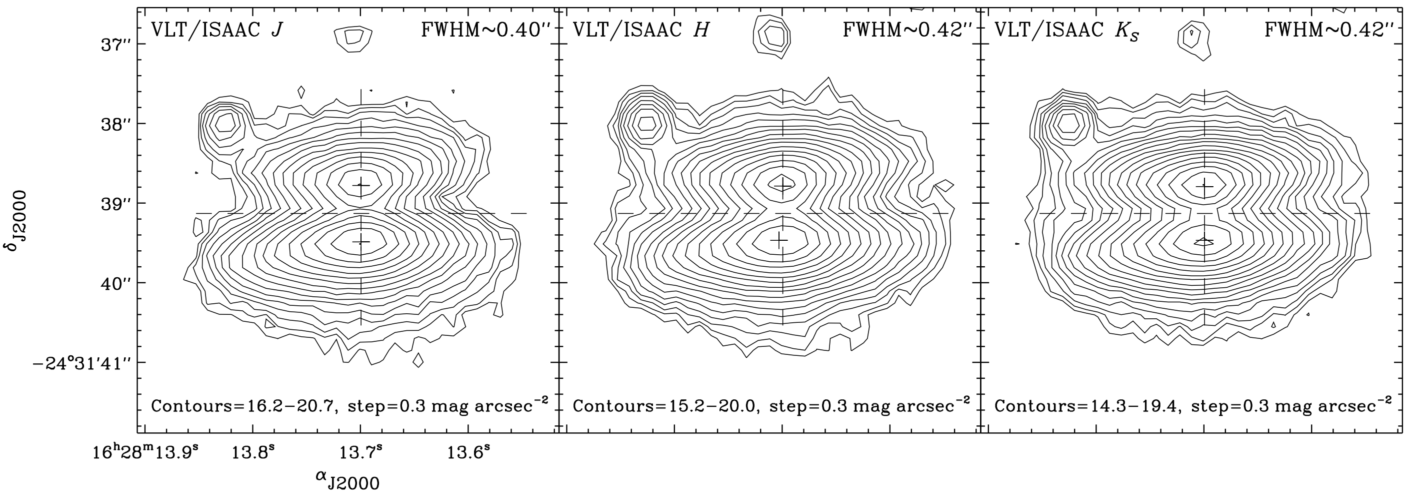

FIG. 3.— Surface brightness maps of the Flying Saucer from the VLT-UT1/ISAAC observations. We give the calibrated contour intensity range from the peak value to the first contour, with the contour step. The crosses mark the peak positions of the reflection nebulae in each filter. The symmetry axes (dashed lines) are defined from the peak positions in the K_S-band image. Their lengths give the width and the height of the disk.

TABLE 1
OPTICAL/NIR INTEGRATED PHOTOMETRY OF THE FLYING SAUCER.

B_J [a]	B [b]	R_{53F} [a]	R [c]	I [d]	J	H	K_S
20.4±0.3	20.5±0.3	18.6±0.3	18.4±0.3	17.16±0.14	15.93±0.06	14.78±0.05	13.98±0.03

[a] SuperCOSMOS Sky Survey (Hambly et al. 2001).

[b] Derived from B_J (Kodak IIIa-J plate + GG395 filter) using the color correction of Blair & Gilmore (1982) assuming the color index $V-R$ corresponding to $T_{\rm eff}=3500$ K in the MK temperature scale (Cox 2000). This leads to $V=19.9$ (marked with a white dot in Fig. 3).

[c] Derived from R_{53F} (Kodak IIIa-F plate + RG630 filter) using the color corrections of Bessel (1986) with I given by DENIS (Epchtein et al. 1999).

[d] DENIS photometry (M. H. Vuong, private communication).

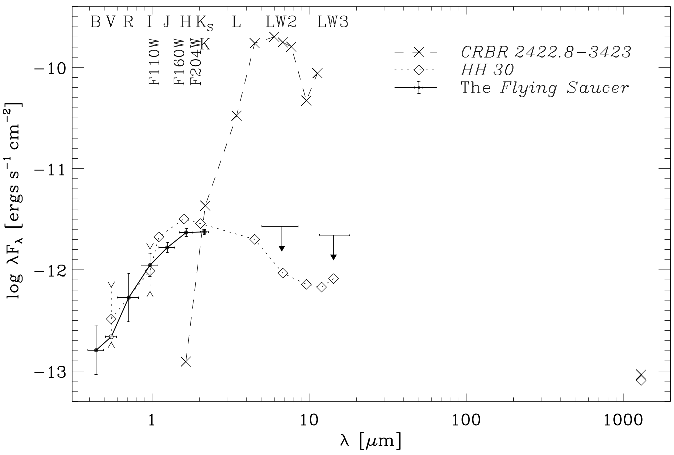

FIG. 4.— Spectral energy distributions (SED) of the Flying Saucer compared to others circumstellar disks. The continuous line and the dots show the SED of the Flying Saucer with two-sigma error bars. (The white dot is only an estimate of the V-band magnitude, see note b of Table 1.) The SED of CRBR 2422.8-3423 located in one of the dense core of the ρ Ophiuchi cloud (Brandner et al. 2000), and HH 30 IRS located in the Taurus dark cloud, are plotted for comparison.

Since the FS falls outside the region mapped in the millimetric continuum by Motte, André, & Neri (1998) we cannot have a direct measurement of the amount of circumstellar material. An estimate of the disk mass will be given from scattered light model in §6.

4. FOREGROUND VISUAL EXTINCTION

To estimate the foreground visual extinction of our object, A_V, we have to deredden its integrated NIR colors, derived from the integrated magnitudes established in the previous section. Meyer, Calvet, & Hillenbrand (1997) observed in Taurus-Auriga that *dereddened* Classical T Tauri stars (CTTS) follow a narrow segment locus in a $J-H, H-K$ color-color diagram. We adopt this locus as statistically representative of the CTTS colors. We stress that an estimate of A_V based on these typical CTTS colors is however only indicative because the NIR light of the FS is almost purely scattered. Its color might then be quite different from that of a typical CTTS in which one primarily sees direct light from the stellar photosphere and the inner disk. The color transformation of the CTTS color locus from the CIT to the 2MASS photometric system using Carpenter (2001) leads to:

$$(J-H)_0 = 0.61 \pm 0.12\,(H-K_S)_0 + 0.50 \pm 0.07\,. \quad (1)$$

Meyer, Calvet, & Hillenbrand (1997) used the extinction law from Cohen et al. (1981), without taking into account its uncertainties, to deredden their CTTS sample. To be

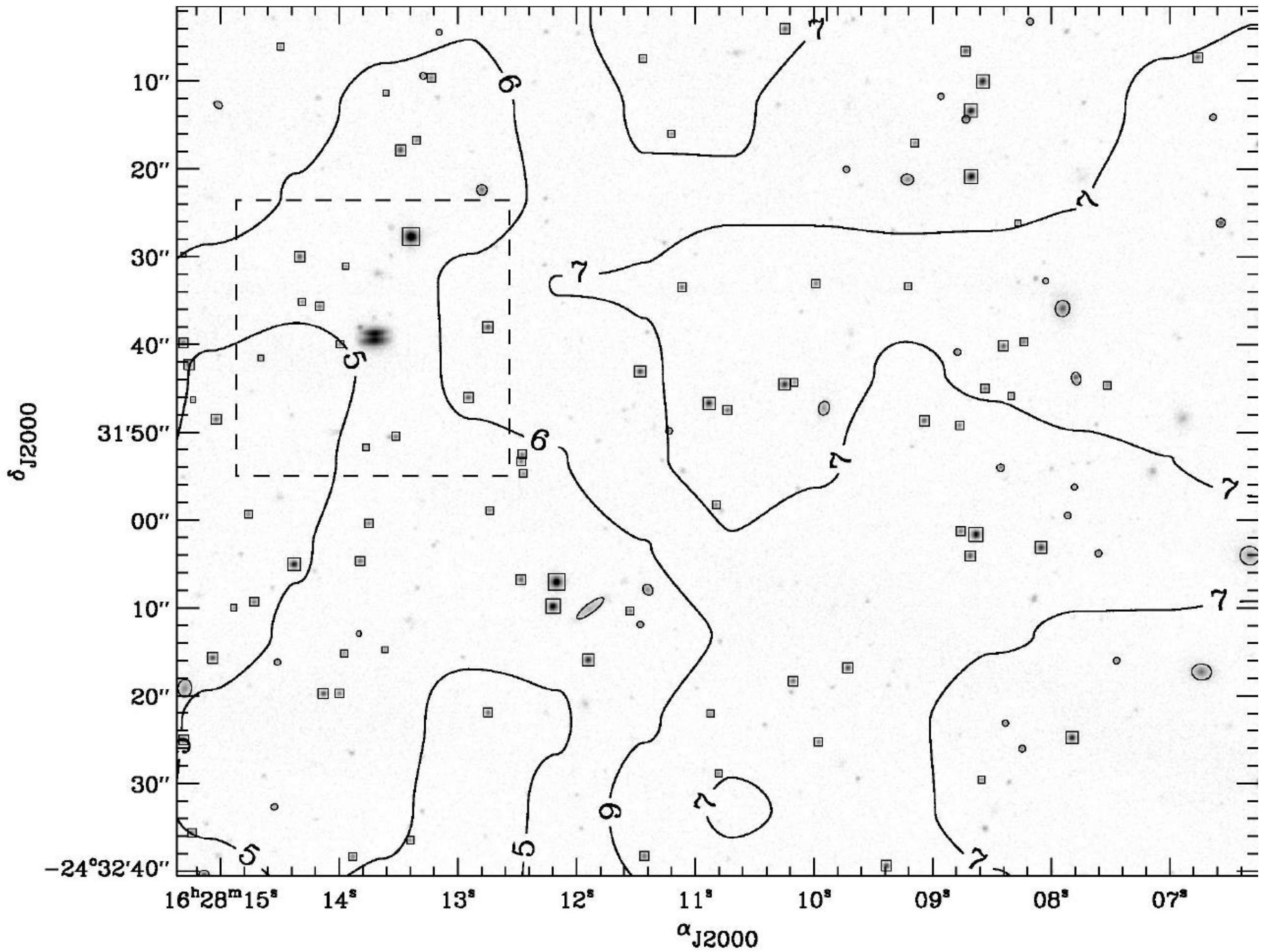

FIG. 5.— Extinction map of the area around the Flying Saucer. The background image is the K_S-band VLT-UT1/ISAAC image displayed using a logarithmic color stretch. The dashed box corresponds to the area of Fig. 2. Squares and ellipses mark stars and galaxies, respectively, with signal-to-noise greater than 5, selected using SExtractor (Bertin & Arnouts 1996). Contours show the extinction map computed from the colors of the selected (background) stars. Contour labels give the visual extinction in magnitude.

consistent with their results we take the same extinction law transformed to the 2MASS photometric system:

$$(J-H)-(J-H)_0 = 0.118 \pm 0.001\,A_V, \qquad (2)$$

$$(H-K_S)-(H-K_S)_0 = 0.067 \pm 0.001\,A_V, \qquad (3)$$

which leads to $E(J-H)/E(H-K_S) = 1.77 \pm 0.04$. Straightforward algebra with formulae 1–3 using the observed NIR colors ($J-H = 1.15 \pm 0.08$ mag, $H-K_S = 0.80 \pm 0.06$ mag), and combining the quoted uncertainties, gives A_V=2.1±2.6 mag (see Fig. 6).

In order to obtain an upper limit on the foreground visual extinction of the FS, we computed the extinction map of the area around it by applying the "Near Infrared Color-Excess" (NICE) method (Lada et al. 1994; Alves et al. 1998). We extracted with SExtractor (Bertin & Arnouts 1996) sources with signal-to-noise greater than 5 in the three filters. To compute this map we selected only sources with stellarity indexes greater than 0.95 (other sources were considered as galaxies). Because there were no observations of the unreddened background stellar field (necessary for the determination of the zero point of the extinction scale), we must adopt a $< H-K_S >$ color for this background. Alves et al. (1998) found $< H-K_S >$ $= 0.20 \pm 0.13$ mag towards a complex region in Cygnus, essentially at the Galactic plane, while Alves, Lada, & Lada (2001) found $< H-K_S > = 0.12 \pm 0.08$ mag towards a clean line-of-sight towards the Galactic bulge, at $b \simeq 7°$. The stellar background towards the Ophiuchus complex is probably even better behaved, because it lies at $b \simeq 15°$. On the other hand, the $< H-K_S >$ color of the North Galactic pole from 2MASS data is also ∼0.12 mag (M. Lombardi, private communication), so we decided to adopt this as the mean Ophiuchus background color.

We show our extinction map in Fig. 5. The spatial resolution of the map is 20″, and the visual extinction ranges from 5 to 7 mag. The extinction increases from East to West, i.e. towards the molecular core (see Fig. 1), hence tracing the presence of material related with the main cloud. This extinction map leads to the following upper limit on the foreground extinction of the FS: $A_V \leq 5.1 \pm 1.2$ mag. Our previous estimate based on the CTTS colors, A_V=2.1±2.6 mag, is consistent with this upper limit, and might imply that the FS is located within this peripherical material, which is not unreasonable. We adopt this extinction value as our best guess.

Thanks to its location at the periphery of the dense cores, this disk suffers less foreground extinction than the other disks already found in this star-forming region. This is also visible in Fig. 3 where its SED shows only a slow rise at short wavelength in contrast to the steep rise of CRBR 2422.8-3423 due to the high extinction of dense cores (Brandner et al. 2000). Cotera et al. (2001) found a comparable foreground visual extinction for HH 30 IRS ($A_V \leq 4.1 \pm 0.9$ mag) assuming a typical stellar type M0 for the central star. Since the FS suffers no background emission from the dense cores, it is an ideal laboratory for the study of both dust and gas in circumstellar disks.

5. PIXEL NIR COLOR MAPPING OF THE REFLECTION NEBULAE

We noted in the previous section the reddish appearance of the northern reflexion nebula of the FS, appearing in Fig. 2. To our knowledge such a NIR color difference between the reflexion nebulae of an edge-on disk has never been observed. NIR adaptive optics images of HK Tau/c display only a "slight change in the nebula's appearance between J and K" (Stapelfeldt et al. 1998); speckle imaging shows that the flux ratio between the two nebulae increases from 5 at J to 8 at K (Koresko 1998). To do a spatially resolved quantitative study of the NIR color differences between the two nebulae of the FS, we introduce a new NIR data visualization method called "Pixel NIR color mapping", PICMap for short. Although in this paper we apply it to the NIR photometry of the FS, this method is general and could conceivably be applied to other photometric bands and adapted to other spatially resolved objects.

The central idea is the following. We want to visualize directly in a single VLT image the $J-H$ and $H-K_S$ colors of each pixel of the FS. We start by selecting the pixels of the FS located inside the boundary of the aperture photometry defined in §3 (see the upper left-panel of Fig. 6), and by computing their $J-H$ and $H-K_S$ colors from the J, H and K_S brightness maps of Fig. 3. Then we plot this set of $J-H$ and $H-K_S$ colors in a $J-H, H-K_S$ color-color diagram, much in the way the NIR colors of individual stars in an association would be plotted. By analogy, we also plot in this diagram the standard ISM reddening vector. The upper right-hand panel of Fig. 6 illustrates the main result: most of the pixels in the $J-H, H-K_S$ diagram are found to be spread roughly along the reddening vector. Therefore, we use its direction to build an arbitrary color palette, shown to the right of the diagram. The last step of the method is then to create a mapping, both on the $J-H, H-K_S$ diagram and on the VLT image, by "coding" the color of each FS pixel according to its projection on this color palette. In other words, PICMap defines a correspondence between the $J-H, H-K_S$ plane and the VLT image. As we shall see, this visualization method is powerful to detect any unusual trend in NIR colors within the FS image.

Physically, we could interpret the pixel color palette used in the PICMap as a visualization of the NIR colors of the nebula pixels in terms of pure extinction by interstellar medium type dust grains. We caution however that the grains in the disk may be grayer than interstellar medium type dust grains (see §6.2), and the true extinction along a line-of-sight through the nebulae is then likely considerably higher than the standard extinction derived from this simple ISM extinction law. In reality, the NIR colors of the FS result from a complex combination of extinction and scattering by disk grains, which can only be reproduced by modelling the radiative transfer of the stellar light through the dust, as discussed in the next section. However the PICMap can be used to quantify the relative difference of NIR colors between the two reflection nebulae in term of standard ISM extinction.

In the upper panels of Fig. 6 when one moves in the VLT image from the edge of the southern nebula to the dark lane along the vertical axis of the disk, the corresponding NIR colors in the $J-H, H-K_S$ diagram (white dots) follow roughly the direction of the ISM reddening vector, with an increase of ~4 mag of standard extinction. The same amount of standard extinction is also visible for the NIR colors of the pixels located between the edge of the northern nebula and the dark lane (black dots). However the northern nebula suffers an extra standard extinction of ~3 mag compared to the southern nebula. In the $J-H, H-K_S$ diagram, it is also clear that the NIR colors are at a peak for many pixels of the northern nebula, and display what would be called a "NIR color excess" in the case of young stars. The PICMap method allows to locate them easily spatially on the VLT image. They are not distributed at random in the northern nebula, but form a ridge, 0.″3 (40 AU at 140 pc) to the north of the dark lane and parallel to it. There is no similar feature in the southern nebula.

In spite of the fact that the FS disk is seen nearly edge-on, it is clearly asymmetric with respect to the dark lane, the northern nebula being significantly redder than the southern nebula. In the next section, we will use axisymmetric disk models with radiative transfer, to look for a model parameter set that reproduces the observed NIR color asymmetry. We will apply our PICMap method to the scattered light model, to visualize the results and compare it with our observations.

6. RADIATIVE TRANSFER MODELS

We adopt a axisymmetric density structure for the circumstellar material (i.e. symmetric with the disk midplane), with dust grains that reproduce the images and spectral energy distribution (SED) of HH30 IRS, and perform the radiative transfer simulation using Monte Carlo techniques (e.g., Whitney & Hartmann 1992; Code & Whitney 1995) to compare scattered light models with the high resolution VLT images. For calculating synthetic SED, we use the Monte Carlo radiative equilibrium technique of Bjorkman & Wood (2001) as adapted for T Tauri disks (Wood et al. 2002a, b).

6.1. *Density structure of the circumstellar material*

6.1.1. *Disk model*

As with previous models of disk SEDs and scattered light images, we adopt a axisymmetric flared disk structure in which the total density (gas plus dust) is:

$$\rho_{\rm disk} = \rho_0 \left(\frac{R_\star}{\varpi}\right)^\alpha \exp\left(-\frac{z^2}{2\,h^2(\varpi)}\right), \qquad (4)$$

where ρ_0 is the disk density extrapolated to the stellar surface (we set $R_\star = 1.03\,{\rm R}_\odot$; see SED model §6.4),

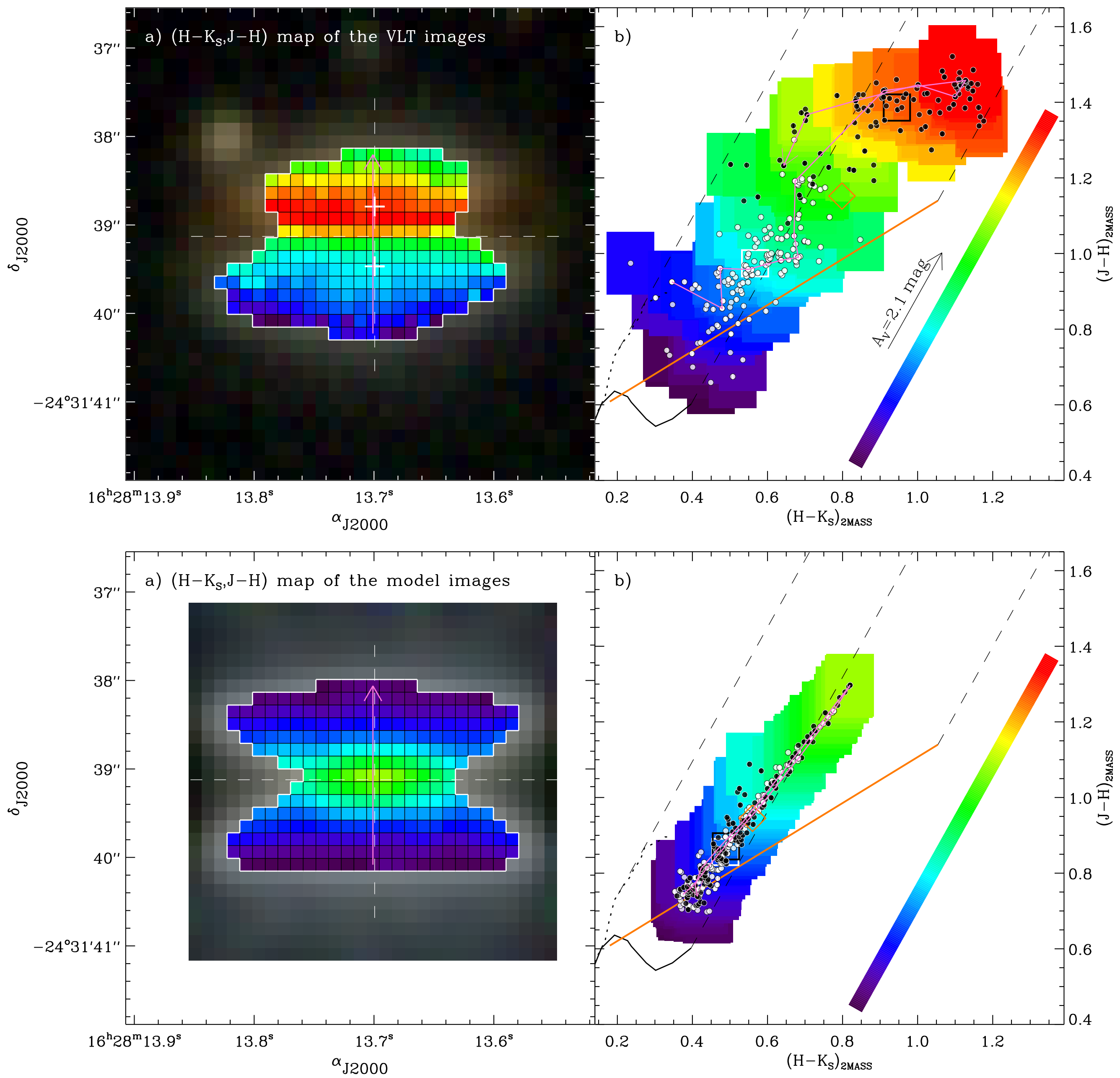

FIG. 6.— Pixel NIR Color Mapping. *Upper panels:* a) $(H - K_S, J - H)$ map of the VLT images. The background image is an enlargement of the color composite image presented in Fig. 2.b, resized to the field of view of Fig. 3. The white crosses mark the peak positions of the reflection nebulae in the K_S-band image, and the dashed lines are the symmetry axes drawn in Fig. 3. The white contour defines the boundary of the aperture photometry defined by surface brightness at least greater than 19.3 mag arcsec^{-2} in the three NIR filters. The color of each pixel of this area is coded according to its position in the $J - H, H - K_S$ diagram on the right-hand panel. The purple arrow shows the path when one moves on the vertical axis of the disk; the corresponding path is also shown in the right-hand panel. b) Corresponding $J - H, H - K_S$ diagram of the nebula pixels (2MASS photometric system). The black and dotted continuous lines show the intrinsic colors of A0–M6 dwarfs and giants (Bessel & Brett 1988), respectively. The orange line is the CTTS locus from Meyer et al. (1997). Reddening vectors (Cohen et al. 1981), adapted for the 2MASS photometric system, are drawn for giants, M6 stars, and CTTS. The orange diamond shows the NIR colors of the integrated light of the disk. The arrow marks the estimate of the disk foreground visual extinction obtained from the CTTS locus (see §4), and gives the extinction scale. The white and black squares mark the NIR colors of the integrated light of the southern and northern nebula, respectively. White and black dots mark the NIR colors of pixels of the southern and northern nebula, respectively. The one-sigma photometric errors are given by the sizes of the error boxes centered on the dots. The color palette defined on the right parameterizes the NIR colors of the nebula pixels in terms of simple ISM extinction. The color of the error boxes are coded according to their projections on the color palette. The purple arrow corresponds to the NIR color variations when one moves on the vertical axis of the disk. See detailed discussion of this Fig. in §5. *Lower panels:* a) $(H - K_S, J - H)$ map of the disk plus diffuse infalling envelope model. b) Corresponding $J - H, H - K_S$ diagram of the model image pixels. Symbols are the same than used in the upper panels. The color palette is identical to the one use in the upper panel, allowing easier comparisons between the model predictions and the observations.

ϖ is the radial coordinate in the disk midplane (with $\varpi \geq R_\star$), and the scale height increases with radius, $h(\varpi) = h_0 \, (\varpi/R_\star)^\beta$. We assume that the gas and dust are well mixed throughout the disk. We adopt for the flaring parameter β the value derived in the hydrostatic disk structure models of D'Alessio et al. (1998), $\beta = 5/4$; and set $\alpha = 3(\beta - 0.5) = 9/4$, which is the value appropriate for viscous accretion theory (Shakura & Sunyaev 1973). This leads to a surface density $\Sigma \propto \varpi^{-1}$ (D'Alessio et al. 1998), flatter than the one usually found in the literature ($\Sigma \propto \varpi^{-3/2}$; e.g., Beckwith et al. 1990). The disk outer radius, $\varpi_{\rm out}$, is fixed to 300 AU to match the extent found in the VLT J image. This value is a lower limit of the disk outer radius. In our model the disk is passive, without any source of internal heating. For low mass disks ($M_{\rm disk} << 0.1\,{\rm M}_\odot$), the heating due to accretion luminosity is negligible and stellar irradiation dominates the disk heating (D'Alessio et al. 1998). The light coming out of this system is thus only the light of the star reprocessed by the disk dust grains.

6.1.2. *Diffuse infalling envelope model*

It is necessary to add another circumstellar component because a model featuring only by a disk produces reflection nebulae with a flat hourglass shape, without the rounded tips visible in Fig. 3. Inspired by the modelling of HH 30 IRS (Wood et al. 1998), we have included a diffuse infalling envelope in our model. The envelope structure follows the rotational collapse geometry of Terebey, Shu, & Cassen (1984) in which the total density (gas plus dust) is:

$$\rho_{\rm env} = \frac{\dot{M}_{\rm env}}{4\pi} \left(G M_\star r_{\rm c}^3\right)^{-\frac{1}{2}} \left(\frac{r}{r_{\rm c}}\right)^{-\frac{3}{2}} \left(1 + \frac{\mu}{\mu_0}\right)^{-\frac{1}{2}} \times \left(\frac{\mu}{\mu_0} + \frac{2\mu_0^2 r_{\rm c}}{r}\right)^{-1} , \quad (5)$$

where $\dot{M}_{\rm env}$ is the mass infall rate, $r_{\rm c}$ is the centrifugal radius, $\mu = \cos\theta$ (with θ the polar angle measured from the disk axis), and $\mu_0 = \mu(r \to \infty)$ is determined by

$$\mu_0^3 + \mu_0 \left(\frac{r}{r_{\rm c}} - 1\right) - \mu \, \frac{r}{r_{\rm c}} = 0 \, . \quad (6)$$

For our models we adopt $r_{\rm c} = \varpi_{\rm out} = 300\,{\rm AU}$, $M_\star = 0.5\,{\rm M}_\odot$, and an outer envelope radius of 1000 AU. We also include a curved bipolar evacuated cavity in the envelope. The cavity walls are curved with their height scaling as $z_{\rm cav} \sim \varpi^2$ and a half opening angle of 20° at the outer radius of the envelope.

6.2. *Properties of the disk dust grains*

In young stellar objects, the wavelength dependence of the dust properties are inferred from the slope of the submillimetric continuum emission (e.g., Beckwith et al. 1990; Beckwith & Sargent 1991) and also from the wavelength dependence of the width of dust lanes of edge-on disks (e.g., Cotera et al. 2001). These studies show that opacity laws shallower than the one of the ISM are needed. Indeed for HH 30 IRS, ISM type grains produce very compact images in $K_{\rm S}$ (Wood et al. 1998), without dark lanes. We use the dust grains described in Wood et al. (2002), which reproduce the multi-wavelength images and continuum fluxes for the HH 30 IRS disk. This dust model uses a "power law with exponential cutoff" for the dust size distribution. The exponential scale length for this dust distribution, $a_{\rm c} = 50\,\mu$m, indicates dust grains have grown to larger than $50\,\mu$m within the HH 30 IRS disk.

The parameters for the gas plus dust mixture for the NIR scattered light models are the opacity, κ, albedo, ω, and Henyey-Greenstein scattering asymmetry parameter, g (Henyey & Greenstein 1941), and are shown in Table ??. The opacity for this model varies from $\kappa_J = 24\,{\rm cm}^2\,{\rm g}^{-1}$ to $\kappa_K = 16\,{\rm cm}^2\,{\rm g}^{-1}$, while for the ISM the opacity is larger and has a steeper wavelength dependence with $\kappa_J = 65\,{\rm cm}^2\,{\rm g}^{-1}$ and $\kappa_K = 22\,{\rm cm}^2\,{\rm g}^{-1}$ (e.g., Kim, Martin, & Hendry 1994).

6.3. *Scattered light model of the FS*

Having set up the circumstellar material density structure and dust grain properties as used for modelling other circumstellar disks, we compute a synthetic scattered light image at λ=1.25 μm, convolved with a 0.″4-FWHM Gaussian point spread function. We do not include additional noise. We vary the disk inclination, i, the disk scale height, h_0, disk mass, $M_{\rm disk}$, and envelope accretion rate $\dot{M}_{\rm env}$ until we reproduce the VLT J image. Then we make scattered light models for the central wavelengths of the H and $K_{\rm S}$ filter. The intrinsic luminosity and spectrum of the central star is not set in this calculation. Instead the model surface brightness is normalized in each filter using the peak surface brightness of the southern nebula. Among all the free parameters of our model we note that only the disk inclination could produce an asymmetry between the two reflection nebulae in the resulting scattered light images.

Figure 7 shows our simulation for a 300 AU outer radius disk viewed at $i = 86°$ with $h_0 = 0.015\,{\rm R}_\star$, giving h(100 AU)=15.3 AU, and $M_{\rm disk} = 2\,10^{-3}\,{\rm M}_\odot$. For comparison Wood et al. (2002) find using the same modelling a similar disk mass for HH 30 IRS with $M_{\rm disk} = 1.5\,10^{-3}\,{\rm M}_\odot$. From the various models computed with the gas plus dust mixture parameters as given in Table ?? we estimate the following uncertainties: $\sigma_{\rm i} = 1°$, $\sigma_{\rm h(100\,AU)} = 1\,{\rm AU}$, $\sigma_{\rm M_{disk}} = 0.5\,10^{-3}\,{\rm M}_\odot$. The disk mass we derive is obviously sensitive to the dust grain properties. For instance for fixed values of ω and g, what is really determined from the modelling is the product of disk mass and opacity. If we were to use a different dust opacity the disk mass would scale according to that. Moreover the disk mass is a lower limit since the opacity is not sensitive to very large particles such as rocks, planetesimals, or planets. The envelope is very tenuous, with a total mass $M_{\rm env} = 4 \times 10^{-4}\,{\rm M}_\odot$. The envelope accretion rate is very weak with $\dot{M}_{\rm env} = 10^{-7}\,{\rm M}_\odot\,{\rm yr}^{-1}$. For comparison typical envelope accretion rates of evolved protostars, Class I sources (Lada 1991), are larger with $\dot{M}_{\rm env} = (2$–$10) \times 10^{-6}\,{\rm M}_\odot\,{\rm yr}^{-1}$ (Strom 1994; Kenyon et al. 1993; Whitney, Kenyon, & Gomez 1997), whereas CTTS have $\dot{M}_{\rm disk} = 10^{-8}$–$10^{-6}\,{\rm M}_\odot\,{\rm yr}^{-1}$ (Strom 1994, and references therein). The circumstellar material of the FS is thus characteristic of a CTTS. Our symmetric disk model reproduces correctly the North-South extent of the FS in the

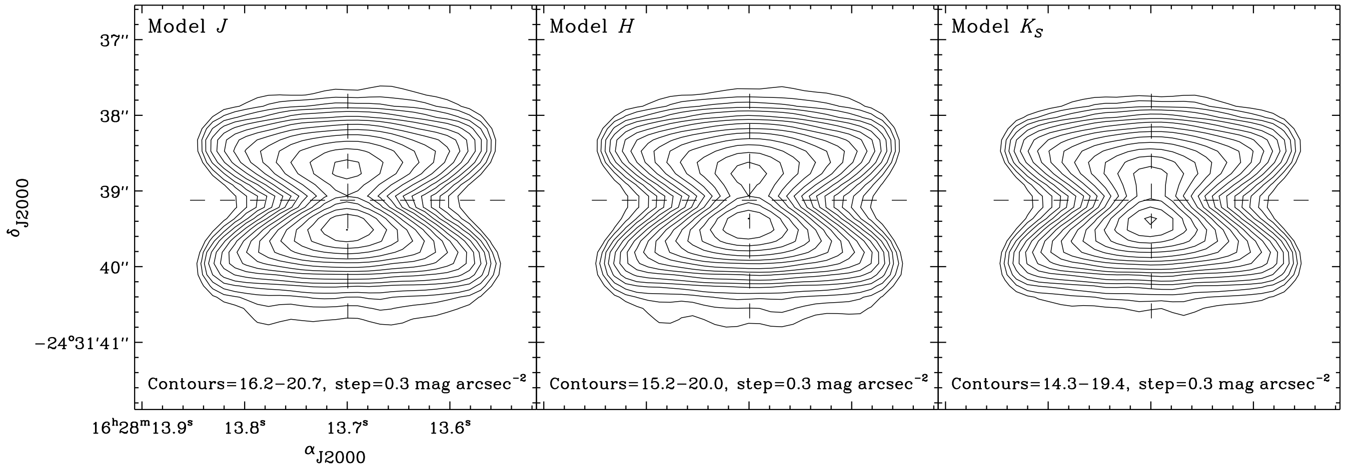

FIG. 7.— Surface brightness maps of our disk model (see text for the parameter values).

three bands thanks to this diffuse infalling envelope, and the East-West shape of the southern nebula. However the width of the northern nebula appears $\sim 25\%$ larger than in the VLT data. A smaller inclination ($\sim 80°$) improves the match with the observation by reducing the width of the northern nebula, but decreases also dramatically its peak brightness leading to a more important discrepancy.

There are also discrepancies between our axisymmetric model and the VLT observation as we go to longer wavelengths. In particular the width of the dark lane is reproduced only in the J-band. At longer wavelengths the width of the dark lane in the axisymmetric models decreases as the dust opacity decreases, and the brightness of the northern nebula is always less than that of the southern nebula (e.g., Wood et al. 1998). However, the VLT data show no variation of the width of the dust lane with the wavelength, and moreover as already noted in §3 the northern nebula brightness relative to the southern nebula brightness *increases*. A steeper grain size distribution and/or smaller maximum grain size may explain the absence of variation of the width of the dark lane at NIR (D'Alessio, Calvet, & Hartmann 2001), but cannot reproduce the brightening of the northern nebula. The determination of an adapted dust opacity law for this object is beyond the scope of this paper, and should be inferred using complementary observation made at longer wavelengths, more constraining for the dust size distribution (e.g., Wood et al. 2002).

The lower panels of Fig. 6 shows the resulting PICMap for our model. We can see easily with this tool that the NIR color distribution of the southern nebula along the reddening vector is quite well reproduced, however the NIR color distribution of the two nebulae is nearly symmetric with the dark lane. We conclude that the *axisymmetric* disk model does not reproduce the asymmetry in the color spatial distribution observed in the scattered light of the FS.

6.4. *SED model of the FS*

Since the spectral type of the central star is unknown, we have assumed $T_{\rm eff} = 3500\,{\rm K}$, and used the corresponding Kurucz atmosphere model (Kurucz 1994) for the input stellar spectrum. As the envelope has a small mass compared to the disk mass, distributed throughout a much larger volume than the denser disk, we neglect it and we compute the synthetic emergent SED from our symmetric disk model only. We apply the foreground visual extinction estimated in §4 using the analytical fits from optical to IR of the extinction cross-section given by Ryter (1996), combined with the canonical relation between visual extinction and column density obtained by Predehl & Schmitt (1995). Adopting a source distance $d = 140\,{\rm pc}$ we require that $L_\star = 0.14\,{\rm L}_\odot$ (which corresponds to $R_\star = 1.03\,{\rm R}_\odot$) to reproduce both the optical and the NIR fluxes (Fig. 6.4). Below $2\,\mu$ the SED is dominated by the (scattered) light of star, while at longer wavelengths the emission from the disk dust grains dominates. Varying the disk inclination from pole-on to edge-on reduces the flux because the disk midplane is optically thick in the MIR. Our SED simulation predicts 10–20 μm fluxes of 0.7–1.8 mJy, and 1.3 mm fluxes of 12.5 mJy.

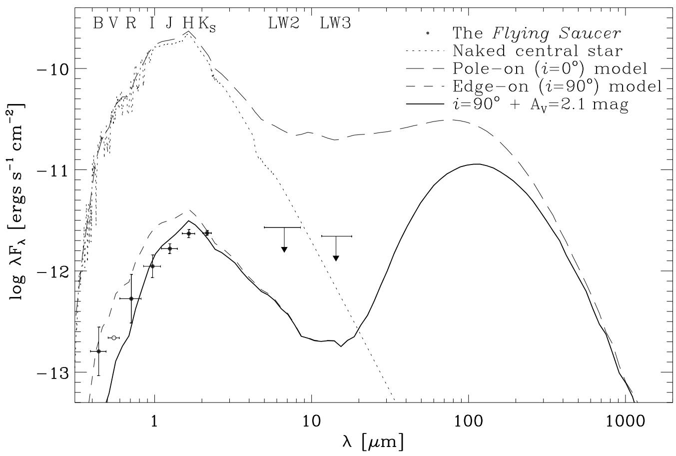

FIG. 8.— Spectral energy distribution for the Flying Saucer model. The black dots mark the observed optical and NIR fluxes with two-sigma error bars. (The white dot is only an estimate of the V-band magnitude, see note b of Table 1.) The continuous line shows our best model: an edge-on disk (short-dashed line) plus 2.1 mag foreground visual extinction. The dotted line is the Kurucz atmosphere model for $T_{\rm eff} = 3500\,{\rm K}$ taken as the spectrum of the central star. The long-dashed line is the emergent SED when the disk is viewed pole-on.

7. DISCUSSION

The spatial study of circumstellar disk is usually based only on surface brightness maps as in Fig. 3. Thanks to the high spatial resolution achieved with our VLT NIR observations (0.″4-seeing images), we have been able to make a spatial study of the NIR colors of the individual pixels of the two resolved reflection nebulae of this nearly edge-on disk. We introduced in this paper a new NIR data visualization called "Pixel NIR color mapping" (PICMap for short), to visualize directly the NIR colors of the nebula pixels. This is a power tool to identify and localize any unusual NIR color trend in the reflection nebulae. We have found with it a NIR color excess and an extra standard extinction in the northern reflection nebula. Fitting the images and the SED with axisymmetric disk model leads to model parameters consistent with what would be expected for a typical CTTS, but cannot reproduce the observed NIR colors. It is necessary to introduce a source of asymmetry in our axisymmetric modelling.

We use in our model a uniformly bright star. There could be cool or dark spots on the star that will change the illumination pattern and consequently the brightening of the northern nebula. Stellar hotspot models produce a typical lighthouse effect, which has been proposed to explain the observed brightening and dimming of the reflection nebulae in HH 30 IRS (Wood & Whitney 1998). However such a phenomenon should produce changes at least on a stellar rotation period (∼few days), it is thus unlikely to be observed at the same phase on a 130 day time interval. We could have an embedded shock associated with a micro-jet, which could emit H_2 lines producing the brightening in H and K_S (e.g., Grosso et al. 2001). However there is no evidence in this object of H_2 emission knots outside the nebulae. This micro-jet hypothesis in the northern nebula can be easily tested with NIR spectroscopy and narrow band filter imaging.

We could account for the lower brightness of the northern nebula at short wavelengths and its redder infrared color as due to ~ 3 mag of localized foreground extinction. From the color-color diagram of the model image (see lower right-hand panel of Fig. 6), we note that adding an extra extinction of ~ 3 mag only in front of the northern nebula reproduces the observed range of $J-H$ colors. However this localized foreground extinction is not visible in our extinction map (Fig. 5). Adding ~ 3 mag foreground extinction only above the dark lane can only be an ad hoc solution. A more natural way to explain these differences would be to introduce an extra self-absorption, possibly due to a large-scale disk warp. For instance Launhardt & Sargent (2001) have detected the millimeter range the presence of a symmetric 20° warp beyond 120 AU in an ~ 200 AU-radius edge-on disk. If a such large-scale disk warp is seen in front of the central star, it could strongly affect the scattered light. Scattered light models of warped disks are now needed to obtain quantitative predictions. This idea would be fruitful to test in detail, as a large-scale disk warp may be excited by a planet on an inclined orbit (e.g., Lubow & Ogilvie 2001).

We stress that our axisymmetric model assumes that the dust and gas are well mixed, it does not take into account the settling of the larger grains in the disk mid-plane. Moreover, having no observational constraints at longer wavelengths, we use conservatively a gas plus dust mixture that reproduces the images and SED of HH30 IRS. Other grain properties combined with dust settling might possibly account for some of the observed color gradient.

In summary, while we can reproduce many of the features of the FS using a symmetric disk plus envelope, our models should be extended to include non-symmetric geometries, specific dust properties, and dust settling, to explain the shortcomings of the model we have presented. The PICMap method introduced in this paper is a power tool to compare the predictions of these improved models with the strong spatial constraints brought by our observations. A more extensive coverage of the SED of the FS from NIR to MIR and millimetric, combining ground and space observations (e.g., HST, VLT/NACO-LGS, SIRTF, Plateau de Bure Interferometer), will further help to constrain the dust properties (e.g., D'Alessio, Calvet, & Hartmann 2001; Wood et al. 2002) and the disk structure of this object.

We would like to thank the referee, Chris Koresko, for having delivered rapidly his report, and for suggestions and comments that improved the final manuscript. We also thank the Director of ESO, Catherine Cesarsky, who gave us a part of her discretionary time to carry out this work, the anonymous observer who triggered the VLT service mode observation, and Anne Dutrey, François Ménard, and Barbara Whitney for useful discussions. We acknowledge financial support from the European Union (HPMF-CT-1999-00228; N. G.); the PPARC Advanced Fellowship (K. W.); the BMBF (DLR grant 50 OR 0003; R. N.); the NASA's Long Term Space Astrophysics Research Program (NAG5 3248; J. E. B.), and the National Science Foundation (AST 9819928; J. E. B.). This publication makes use of data products from the Two Micron All Sky Survey, which is a joint project of the University of Massachusetts and the Infrared Processing and Analysis Center/California Institute of Technology, funded by the NASA and the National Science Foundation. We also used the SuperCOSMOS Sky Survey of the Institute for Astronomy, Royal Observatory, Edinburgh.

REFERENCES

Abergel, A., Bernard, J. P., Boulanger, F., et al. 1996, A&A, 315, L329
Allen, L. E., Myers, P. C., Di Francesco, J., et al. 2002, ApJ, 566, 993
Alves, J., Lada, C. J., Lada, E. A., et al. 1998, ApJ, 506, 292
Alves, J., Lada, C. J., & Lada, E. A. 2001, Nature, 409, 159
Beckwith, S. V. W., Sargent, A. I., Chini, R. S., & Guesten, R. 1990, AJ, 99, 924
Beckwith, S. V. W. & Sargent, A. I. 1991, ApJ, 381, 250
Bertin, E. & Arnouts, S. 1996, A&AS, 117, 393
Bessell, M. S. 1986, PASP, 98, 1303
Bessell, M. S. & Brett, J. M. 1988, PASP, 100, 1134
Bjorkman, J. E.& Wood, K. 2001, ApJ, 554, 615
Blair, M. & Gilmore, G. 1982, PASP, 94, 742
Bontemps, S., André, P., Kaas A. A., et al. 2001, A&A, 372, 173
Boss, A. P. & Yorke, H. W. 1996, ApJ, 469, 366
Brandner, W., Sheppard, S., Zinnecker, H., et al. 2000, A&A, 364, L13
Burrows, C. J., Stapelfeldt, K. R., Watson, A. M., et al. 1996, ApJ, 473, 437
Carpenter, J. M. 2001, AJ, 121, 2851
Code, A. D. & Whitney, B. A. 1995, ApJ, 441, 400
Cohen, J. G., Persson, S. E., Elias, J. H., & Frogel, J. A. 1981, ApJ, 249, 481

Cotera, A. S., Whitney, B. A., Young, E., et al. 2001, ApJ, 556, 958
Cox, A. N. 2000, Allen's astrophysical quantities, 4th ed., Cox, A. N. (ed.), Springer
Cutri, R., Skrutskie, M. F., Van Dyk, S., et al. 2000, http://www.ipac.caltech.edu/2mass/releases/second/doc/
D'Alessio, P., Canto, J., Calvet, N., & Lizano, S. 1998, ApJ, 500, 411
D'Alessio, P., Calvet, N., & Hartmann, L. 2001, ApJ, 553, 321
Epchtein, N., Deul, E., Derriere, S., et al. 1999, A&A, 349, 236
Grosso, N., Alves, J., Neuhäuser, R., & Montmerle, T. 2001, A&A, 380, L1
Hambly, N. C., McGillivray, H. T., Read, M. A., et al. 2001, MNRAS, 326, 1279
Henyey, L. C., & Greenstein, J. L. 1941, ApJ, 93, 70
Kenyon, S. J., Whitney, B. A., Gomez, M., & Hartmann, L. 1993, ApJ, 414, 773
Kim, S.-H., Martin, P. G., & Hendry, P. D. 1994, ApJ, 422, 164
Koresko, C. D. 1998, ApJ, 507, L145
Kurucz, R. 1994, Solar abundance model atmospheres, Smithsonian Astrophysical Observatory, CD-ROM 19
Lada, C. J. 1991, in The Physics of Star Formation and Early Stellar Evolution, NATO ASI, C. J. Lada & N. D. Kylafis (eds.), Kluwer, p. 329–363
Lada, C. J., Lada, E. A., Clemens, D. P., & Bally, J. 1994, ApJ, 429, 694
Launhardt, R. & Sargent, A. I. 2001, ApJ, 562, L173
Lubow, S. H. & Ogilvie, G. I. 2001, ApJ, 560, 997
Meyer, M. R., Calvet, N., & Hillenbrand, L. A. 1997, AJ, 114, 288
Motte, F., André, P., & Neri, R. 1998, A&A, 336, 150
Persson, S. E., Murphy, D. C., Krzeminski, W., et al. 1998, AJ, 116, 2475
Predehl, P. & Schmitt, J. H. M. M. 1995, A&A, 293, 889
Ryter, C. E. 1996, Ap&SS, 236, 285
Shakura, N. I. & Sunyaev, R. A. 1973, A&A, 24, 337
Stapelfeldt, K. R., Krist, J. E., Ménard, F., et al. 1998, ApJ, 502, L65
Stapelfeldt, K. & Moneti, A. 1999, in The Universe as Seen by ISO, ESA SP-427, P. Cox & M. F. Kessler (eds.), p. 521–524
Strom, S. E. 1994, Revista Mexicana de Astronomia y Astrofisica, vol. 29, 23
Terebey, S., Shu, F. H., & Cassen, P. 1984, ApJ, 286, 529
Terebey, S., van Buren, D., Hancock, T., et al. 2001, in From Darkness to Light, Origin and Evolution of Young Stellar Clusters, ASP Conf. Ser. 243, Montmerle, T. & André, P. (eds.), p. 243–252
Whitney, B. A. & Hartmann, L. 1992, ApJ, 395, 529
Whitney, B. A., Kenyon, S. J., & Gomez, M. 1997, ApJ, 485, 703
Wilking, B. A. & Lada, C. J. 1983, ApJ, 274, 698
Wood, K. & Whitney, B. 1998, ApJ, 506, L43
Wood, K., Kenyon, S. J., Whitney, B., & Turnbull, M. 1998, ApJ, 497, 404
Wood, K., Wolk, S. J., Stanek, K. Z., et al. 2000, ApJ, 542, L21
Wood, K., Wolff, M. J., Bjorkman, J. E., & Whitney, B. 2002, ApJ, 564, 887